Biochemical and Biophysical Research Communications 780 (2025) 152469

Contents lists available at ScienceDirect

Biochemical and Biophysical Research Communications

journal homepage: www.elsevier.com/locate/ybbrc

# Exploiting ALDH1A2 and ALDH1A3 isoform variability for crystallisation screening

Sonia Siragusa [a], Silvia Garavaglia [a,*], Marco Mazzorana [b,c,**]

[a] Department of Scienze del Farmaco, University of Piemonte Orientale, Via Bovio, 6, Novara, 28100, Italy
[b] Diamond Light Source, Ltd. – Harwell Science and Innovation Campus, Didcot, OX11 0DE, UK
[c] Research Complex at Harwell – Rutherford Appleton Laboratory, Harwell, OX11 0FA, Didcot, UK

ARTICLE INFO

*Keywords:*
ALDH1A2
ALDH1A3
Structure-based drug discovery
Aldehydes
Cancer stem cells

ABSTRACT

Members of the human aldehyde dehydrogenase family 1 (ALDH1As) play a crucial role in converting retinal to retinoic acid, a multifunctional bioactive compound. Most evidence highlight ALDH1As as markers for cancer stem cells correlating with tumour aggressiveness. Increasing structural and biochemical data about these important isoenzymes have been reported in literature. Crystal structures of human ALDH1A2 have been so far only obtained in the presence of ligands/cofactors from vapour diffusion hanging drops. Apo-enzyme structures have been described only for the other two members of the family (ALDH1A1 and ALDH1A3) serving as the basis for their co-crystallisation with various ligands.

In this study, we describe the first apo-ALDH1A2 structure obtained from nanolitre sitting-drop crystallisation, which expands the potential for high-throughput structure-based drug discovery studies on this isoform. We also explore the crystallisability of $NAD^+$-ALDH1A3 from microlitre drops and compare the structure obtained from it with that of apo-ALDH1A2.

Finally, we propose strategies compatible with robotic setups to streamline structural studies on ALDH1A3 and facilitate the exploration of extensive ligand libraries.

## 1. Introduction

Aldehydes are a class of highly reactive toxic compounds, that originate from two primary sources: endogenous, produced by metabolic processes within the body, and exogenous, introduced in the body via environmental exposure [1]. Aldehyde dehydrogenases (ALDHs) are a class of $NAD^+$-dependent enzymes essential for detoxifying aldehydes by oxidising them into carboxylic acids. The ALDHs superfamily is evolutionarily ancient, and is conserved across a wide range of organisms, from bacteria to humans. The structural similarity of these enzymes underpins a common ancestral gene dating back about 3 billion years [2,3]. The nomenclature of ALDHs isozymes was established based on sequence similarity during the 1998 International Symposium on Enzymology [3]. Isozymes within the same family share over 40 % sequence identity, while those in the same subfamily share over 60 % identity [4]. In humans, the ALDH gene family comprises 19 functional proteins and 3 pseudogenes, each distinguished by unique chromosomal locations and substrate specificities [5].

Structurally, ALDHs typically function as dimers or tetramers, with each monomer featuring three key functions: a cofactor-binding domain, a catalytic domain, and oligomerisation domain [6,7]. These domains are spatially arranged to form a funnel-like architecture leading to the catalytic site. Here, isoform-specific amino acids determine substrate selectivity, while conserved residues participate in the catalytic mechanism [8,9]. The reaction begins with the activation of a catalytic Cysteine (Cys320 in ALDH1A2 and 314 in ALDH1A3) by a Glutamic acid (at positions 286 and 280 respectively) and a water molecule, enabling a nucleophilic attack on the aldehyde substrate. This results in the formation of a thiohemiacetal intermediate and the transfer of a hydride to $NAD^+$. The enzyme is subsequently regenerated through hydrolysis of the thioester intermediate, followed by the release of NADH [10].

The human ALDH1A subfamily consists of three members (ALDH1A1, ALDH1A2, and ALDH1A3) that play an important role in the biosynthesis of retinoic acid (RA) [11]. RA, a derivative of vitamin A, is essential for gene regulation, and influences key biological processes such as cell differentiation and development [12]. Its biological role is

* Corresponding author.
** Corresponding author. Diamond Light Source, Ltd. – Harwell Science and Innovation Campus, Didcot, OX11 0DE, UK.
*E-mail addresses:* silvia.garavaglia@uniupo.it (S. Garavaglia), marco.mazzorana@diamond.ac.uk (M. Mazzorana).

https://doi.org/10.1016/j.bbrc.2025.152469
Received 26 January 2025; Received in revised form 21 July 2025; Accepted 8 August 2025
Available online 14 August 2025

mediated through its binding to the nuclear receptors RARs and RXRs, which form complexes that either activate or repress gene expression [13]. This regulatory mechanism is key for embryonic development, particularly in neurogenesis and organ formation, and it is also essential for pluripotent stem cell signalling and immune function [14].

Dysregulation of RA synthesis mediated by ALDH1As has been linked to various diseases including cancer, where altered enzyme activity can promote tumorigenesis [15]. In the case of ALDH1A3, its enzymatic activity can be used as a marker for cancer stem cells and is associated with increased tumour aggressiveness, highlighting the potential for novel isoform-specific therapeutic strategies towards ALDH1As [16].

All ALDH1As share similar molecular architecture, with ALDH1A2 and ALDH1A3 exhibiting 72 % sequence identity. In this context, precise identification of isoform-specific amino acids involved in substrate recognition, is essential for the development of selective inhibitors. High-throughput crystallographic screening offers a promising approach to accelerate the he discovery of isoform-specific compounds [17].

All ALDH1A2 crystal structures published to date have been obtained using microlitre-volume hanging drop crystallisation methods. These structures include complexes with both $NAD^+$ and ligands (PDB: 6ALJ, 6B5G, 6B5H), with a ligand only (PDB: 6B5I), or with $NAD^+$ alone (PDB: 4X2Q) [18]. Notably, all available structures include a ligand ($NAD^+$ or inhibitor), while the apo-form of the enzyme has not been reported yet. This limits the understanding of conformational flexibility and structural changes occurring upon ligand and/or cofactor binding. Such modulations within the active site of the enzyme are critical for rational drug design and for elucidating the enzyme's catalytic mechanism.

To accurately characterise isoform-specific differences in ligand binding, obtaining fully apo- (*i.e.,* $NAD^+$-free) ALDH1A2 crystals is a key priority. In contrast, a large number of crystallographic structures of ALDH1A3 is available. The first ALDH1A3 structure was obtained through co-crystallisation with $NAD^+$ and its reaction product RA (PDB: 5FHZ [8]), providing insights into the substrate and cofactor binding, which are central to its roles in RA biosynthesis and aldehyde detoxification.

Five additional ALDH1A3 structures have been obtained in co-crystallisation with $NAD^+$ and selective inhibitors (PDB: 7A6Q, 6TRY, 6TE5, 6S6W, 6TGW), enabling precise identification of isoform-specific residues involved in ligand selectivity [14,19,20].

Further structural insight was obtained from ALDH1A3 crystals representing distinct enzymatic states including the apo-form (PDB: 7QK7), the $NAD^+$-bound form (PDB: 7QK8), and a complex with ATP (PDB: 7QK9 [21]). However, the crystallisation of both apo- and holo-forms of ALDH1A3 remains highly variable and sensitive to small changes in the experimental geometry and the drop volume. To date, no reproducible methods has been established for obtaining apo-ALDH1A3 crystals.

This hinders the application of soaking techniques which requires unliganded crystals for the introduction of test compounds, consequently slowing down the discovery of potent and selective inhibitors. This challenge may be addressed by co-crystallising the enzyme with low-affinity stabilising molecules that can be later displaced by higher-affinity ligands through soaking.

## 2. Materials and Methods

### 2.1. Molecular biology

The *E. coli* codon-optimised cDNA sequences encoding for the human isoforms of ALDH1A2 (GeneID: 8854) and ALDH1A3 (GeneID: 220) were obtained from GenScript. The N-terminally deleted ALDH1A2 gene (26–518) was cloned into the pET-28b vector between the *Nde*I and *Xho*I sites. An N-terminal $His_6$-tag followed by a TEV protease cleavage site was introduced to generate a $His_6$-TEV-ALDH1A2 construct.

The gene for ALDH1A3 was inserted in pDEST17 vector through the Gateway™ recombination technology, resulting in an N-terminally $His_6$-tagged enzyme (residues 2–513 preceded by an N-terminal tail from the cloning vector). The integrity and correctness of both constructs was confirmed by Sanger sequencing and complete data is reported in Supplementary Materials (Table S1a for ALDH1A2 and S1b for ALDH1A3).

### 2.2. Protein expression and purification

Both proteins were expressed in *E. coli* and purified following protocols optimised based on previous work from our laboratory [8]. Briefly, the plasmids described above were used to transform BL21 CodonPlus (DE3) cells which were grown in LB medium supplemented with appropriate antibiotics (25 μg/mL Chloramphenicol and 100 μg/mL Carbenicillin for ALDH1A3 or 50 μg/mL Kanamycin for ALDH1A2).

Large scale expression was initiated by diluting 1:100 the overnight saturated cultures into baffled Erlenmeyer flasks containing 2xTY medium with antibiotics. Cells were incubated at 37 °C with vigorous shaking (200 rpm) until reaching the optical density of cultures at 600 nm ($OD_{600}$) of 0.8–1. Protein expression was then induced with 1 mM isopropyl β-D-1-thiogalactopyranoside (IPTG) followed by incubation at 18 °C, 200 rpm for 16 h. Cells were harvested by centrifugation at 5000×*g* for 10 min, and the resulting pellet were stored at −80 °C.

For the purification, cells from 1 L of culture were thawed and resuspended at a 1:5 ratio in lysis buffer (50 mM $Na_2HPO_4$, 300 mM NaCl, 1 mM β-mercaptoethanol, 20 mM imidazole, pH 7.5) supplemented with cOmplete™ Protease Inhibitor Cocktail (Roche) and 250 U of Benzonase nuclease. Cells were lysed by two passes through a cell disruptor (Constant systems) at 35 kpsi. The lysate was clarified by ultracentrifugation at 200000×*g* for 30 min at 4 °C, followed by filtration through a 0.22 μm membrane.

The first purification step consisted in an affinity chromatography using a HisTrap FF 1 mL (Cytiva) on a FPLC system. After sample loading, the column was washed with 20 column volumes (CV) of lysis buffer, followed by a 20 CV wash with 20 % elution buffer (50 mM $Na_2HPO_4$, 300 mM NaCl, 1 mM β-mercaptoethanol, 300 mM imidazole, pH 8). Protein were then eluted using a 10 CV linear gradient 20–100 % of elution buffer, and 1 mL fractions were collected.

Protein-containing fractions were diluted 1:3 with size-exclusion chromatography (SEC) buffer (Tris-HCl pH 8, 150 mM NaCl, 10 mM DTT) and concentrated to 5 mL using a 100 kDa MWCO Amicon® Ultra centrifugal filter. This sample was loaded onto a HiLoad 16/600 Superdex 200 column and eluted isocratically, with 1 mL fractions collected. Protein purity was assessed by SDS-PAGE and the purest fractions were pooled and concentrated to 15–20 mg/mL as determined by absorbance at 280 nm using the extinction factors reported in Table S1. Typical yields for purifications from 1 L of cultures were 50 mg for ALDH1A2 and 60 mg for ALDH1A3. Purified proteins, aliquoted in 25 μL volumes, were snap-frozen in liquid nitrogen and stored at −80 °C.

### 2.3. Protein crystallisation

#### 2.3.1. ALDH1A2 high-throughput screening

For *de novo* high-throughput crystallisation screening, ALDH1A2 was thawed on ice for 2 h and diluted with SEC buffer to a concentration of 10 mg/mL. Crystallisation trays were set up using a Mosquito LCP 2 crystallisation robot (STP Labtech) in SWISSCI MRC 3-lens sitting drop crystallisation plates. Drops were prepared at varying protein-to-precipitant ratios: 100 nL + 100 nL, 100 nL + 50 nL, and 50 nL + 100 nL.

To ensure a broad sampling of the crystallisation space, five commercial screens were chosen: Morpheus [22], Wizard 1 + 2, Wizard 3 + 4, Peg Ion, and PGA [23]. The best-diffracting crystals were obtained in the condition reported in Table 1. Crystallisation plates were sealed, incubated at 20 °C and monitored regularly using a Formulatrix imaging system.

**Table 1**
apo-ALDH1A2 crystallisation conditions.

| Crystallisation method | Vapour diffusion (sitting drop) |
|---|---|
| Plate type | SWISSCI MRC 3-lens |
| Temperature (°C) | 20 °C |
| Crystallisation protein | 10 mg/ml |
| Storage-buffer composition | Tris-HCl pH 8, 150 mM NaCl, 10 mM DTT |
| Reservoir composition | 0.09 M NPS, 0.1 M Buffer System 3 (pH 8.5 Tris-base; BICINE 8.5) 30 % v/v Precipitant Mix 3 (20 % v/v Glycerol; 10 % w/v PEG 4000) |
| Drop volume (nL) | 200 (1:1 precipitant: protein ratio) |
| Reservoir volume (μL) | 30 |

### 2.3.2. *ALDH1A3 crystallisation with co-factor*

Following a previously established protocol, ALDH1A3 was thawed on ice, diluted to 7 mg/mL in SEC buffer, and incubated for 30 min after the addition of 1 mM $NAD^+$. Crystallisation trials were set up using 24 wells of a Linbro plates (Jena Bioscience), with each well filled with 500 μL of precipitant solution containing 5 % PEG 400, 100 mM BIS-TRIS (pH 5.5), and 2.2 M ammonium sulfate. Hanging drops were prepared by mixing 1 μL drops of protein solution with 1 μL of precipitant solution on siliconised glass coverslips.

To establish vapour diffusion equilibrium, three different methods were tested: A. Coverslips sealed with Crystal Clear Sealing Tape (Hampton Research, HR3-511) B. Coverslips sealed using a thin layer of DOW CORNING High Vacuum Grease applied around the reservoir edge, C. As in method B, but using DOW CORNING 7 Release Compound Grease instead.

Crystallisation plates were incubated at 20 °C and monitored under a polarised light microscope (Leica M205C equipped with DFC295 camera unit).

## 2.4. *Structure determination and refinement*

Crystals obtained from the various experiments were harvested using SPINE standard cryo-loops and flash-cooled in liquid nitrogen without the addition of cryoprotectants.

X-ray diffraction data were collected at beamline I04 of the Diamond Light Source (UK). Data collection employed a fine-omega slicing strategy (0.1° per image) using a 13 keV X-ray beam. Exposure time and beam attenuation were adjusted to deliver a total radiation dose between 5 and 10 MGy per dataset (Table 2).

The unitial data reduction and integration was performed with the automated pipeline xia2-DIALS [24,25]. Subsequent processing was carried out within the CCP4 Cloud suite [26]: Molecular replacement was conducted using PHASER [27] with curated versions of PDB entries: 4X2Q for ALDH1A2 and 5FHZ for ALDH1A3. Final refinement and preparation of PDBx/mmCIF files for PDB deposition was carried out with Phenix [28,29].

The initial model was refined through iterative cycles of manual model building in Coot [30] alternating with refinement with the programs REFMAC5 [31], applying NCS restraints [32] for all chains in the asymmetric unit. A randomly chosen 5 % subset of reflections were excluded from the refinement of the structure and used for the $R_{free}$ value.

In the final steps of refinement, water molecules were automatically picked using ARP/wARP [33] and manually curated. The $NAD^+$ molecule was manually modelled into the strongest positive density in the $F_o$-$F_c$ difference map. Final refinement statistics and crystallographic parameters are summarised in Table 3.

## 2.5. *Surface plasmon resonance*

Surface plasmon resonance (SPR) experiments were conducted on a Biacore T200 instrument (GE Healthcare) using a NTA sensor chip (see Table 4). ALDH1As subfamily proteins were immobilised via their N-terminal His-tags through nickel-affinity capture. The NTA surface was activated with a 60-s injection of $Ni^{2+}$ solution at a flow rate of 10 μL/min, resulting in a baseline response of about 40 response units (RU), followed by a wash using 3 mM EDTA solution.

His-tagged ALDH1A2 and ALDH1A3 were prepared at concentrations below 10 μM in running buffer to minimise rapid dissociation, and

**Table 2**
Data collection statistics (numbers in parentheses refer to the highest resolution shell).

| | ALDH1A2 | ALDH1A3 |
|---|---|---|
| Beamline | I04 at Diamond Light Source | |
| Energy, Wavelength | 13 keV, 0.9537 Å | |
| Data collection temperature | 100K | |
| Detector | Eiger2 XE 16 M | |
| Rotation range per image | 0.1° | |
| Total rotation per dataset | 360° | |
| Total dose per dataset | 10 MGy | |
| Space group | $P2_1$ a = 82.84, b = 139.48, c = 85.17, α = γ = 90°, β = 93.93° | $P2_1\ 2\ 2_1$ a = 81.03, b = 89.20, c = 158.61, α = β = γ = 90° |
| Resolution limits (Å) | 2.79–72.56 (2.79–2.54) | 2.01–79.33 (2.01–2.04) |
| Total reflections | 341961 (17132) | 77391 (50770) |
| Unique reflections | 47510 (4715) | 72250 (4047) |
| Multiplicity | 7.1 (7.3) | 13.6 (12.5) |
| Completeness (%) | 100.0 (98.2) | 100.0 (99.8) |
| mean(I/sigma(I))* | 5.40 (0.6) | 6.1 (0.4) |
| CC(1/2)* | 1.0 (0.3) | 1.0 (0.3) |
| Wilson B factor ($Å^2$) | 57.97 | 25.69 |

**Table 3**
Refinement and model statistics (numbers in parentheses refer to the highest resolution shell).

| | ALDH1A2 | ALDH1A3 |
|---|---|---|
| Refinement resolution (Å) | 2.80 | 2.5 |
| Rwork (%) | 21.20 | 18.10 |
| Rfree (%) | 28.52 | 23.23 |
| Number of non-hydrogen atoms | | |
| Macromolecules | 14710 | 7678 |
| Ligands | 0 | 6 |
| Water | 53 | 173 |
| RMSD (bonds, Å) | 0.0090 | 0.0073 |
| RMSD (angles, °) | 1.036 | 1.777 |
| Ramachandran plot (%) | | |
| favoured | 92.7 | 95.9 |
| allowed | 6.8 | 3.8 |
| outliers | 0.6 | 0.3 |
| Rotamer outliers (%) | 5.5 | 1.0 |
| Clash score | 16.4 | 2.3 |
| MolProbity score (percentile) | 2.74 | 1.29 |
| Average B-factor | | |
| macromolecules | 69.40 | 35.33 |
| Ligands ($NAD^+$) | – | 60.70 |
| Ligands (others) | – | 44.24 |
| solvent | 56.17 | 42.26 |

**Table 4**
SPR assay results of the interactions between ALDH1A2/ALDH1A3 and $NAD^+$.

| Sample | $K_d$ (μM) | Fit model |
|---|---|---|
| $NAD^+$- ALDH1A2 | 16.8 | Steady-state affinity |
| $NAD^+$–ALDH1A3 | 0.033 | Steady-state affinity |

immobilised over the $Ni^{2+}$-activated surface with 90 injections at a flow rate of 10 μL/min. The running consisted of 5 mM Tris-HCl (pH 8), 150 mM NaCl, 0.5 mM TCEP, 0.05 % P20, 5 % DMSO, and water.

Steady-state binding experiments were performed by injecting $NAD^+$ at various concentrations, prepared through serial seven-fold dilutions of a 500 μM stock, with the lowest concentration being 3.12 μM. Injections were carried out at 30 μL/min and 20 °C. Binding affinities were analysed using a 1:1 interaction steady-state binding model, and data fitting was performed using BIAevaluation 1.0 software (GE Healthcare).

## 3. Results and discussion

The optimised protocol described in the Materials and Methods section enabled large-scale production of human ALDH1A2 and ALDH1A3, yielding over 50 mg/L of culture with purity levels exceeding 95 %.

### 3.1. Rationale for ALDH1A2 crystallisation

The ALDH1A2 crystals described to date have been generated from microlitre-size hanging drop experiments and involved the addition of ligands or cofactors. However, the fully apo form of ALDH1A2 (*i.e.,* free from $NAD^+$ and substrates) has not yet been described. This represents a significant gap in our understanding of the enzyme's structural features and poses a limitation for large-scale drug discovery campaigns against this isoform.

For such applications, it is essential to generate crystals in nanolitre-scale droplets, as demonstrated in this study using SWISSCI MRC3 3-lens plates in combination with a Mosquito liquid-handling robot (SPT Labtech).

In the initial phase of our work, we screened 1440 crystallisation conditions across various commercial precipitant screens. Needle-like crystals were observed in multiple wells, exhibiting variability in size, spatial distribution, and clustering. Fig. 1 shows representative images of the crystallisation plate and resulting crystal morphologies. Detailed conditions for crystals formation across the different screens are provided in Supplementary Fig. S2.

To rapidly identify optimal precipitant conditions and evaluate the effects of buffer composition, pH, and specific salts, X-ray diffraction screening was performed on the apo-enzymes. The most promising crystals were obtained from the Morpheus screen, which consistently yielded high-quality crystals in several wells. In all cases, needle-like morphologies were observed, occasionally displaying crystal twinning (gemination), which could be mitigated by isolating individual crystals during harvesting.

The specific conditions that supported crystal formation are summarised in Table S3 (Supplementary Materials). These results revealed a strong preference for combinations of medium-molecular-weight polyethylene glycols (PEGs) with lighter organic additives such as glycerol and ethylene glycol. The highest-quality crystals were obtained under the Morpheus C11 condition, where the presence of glycerol and PEG

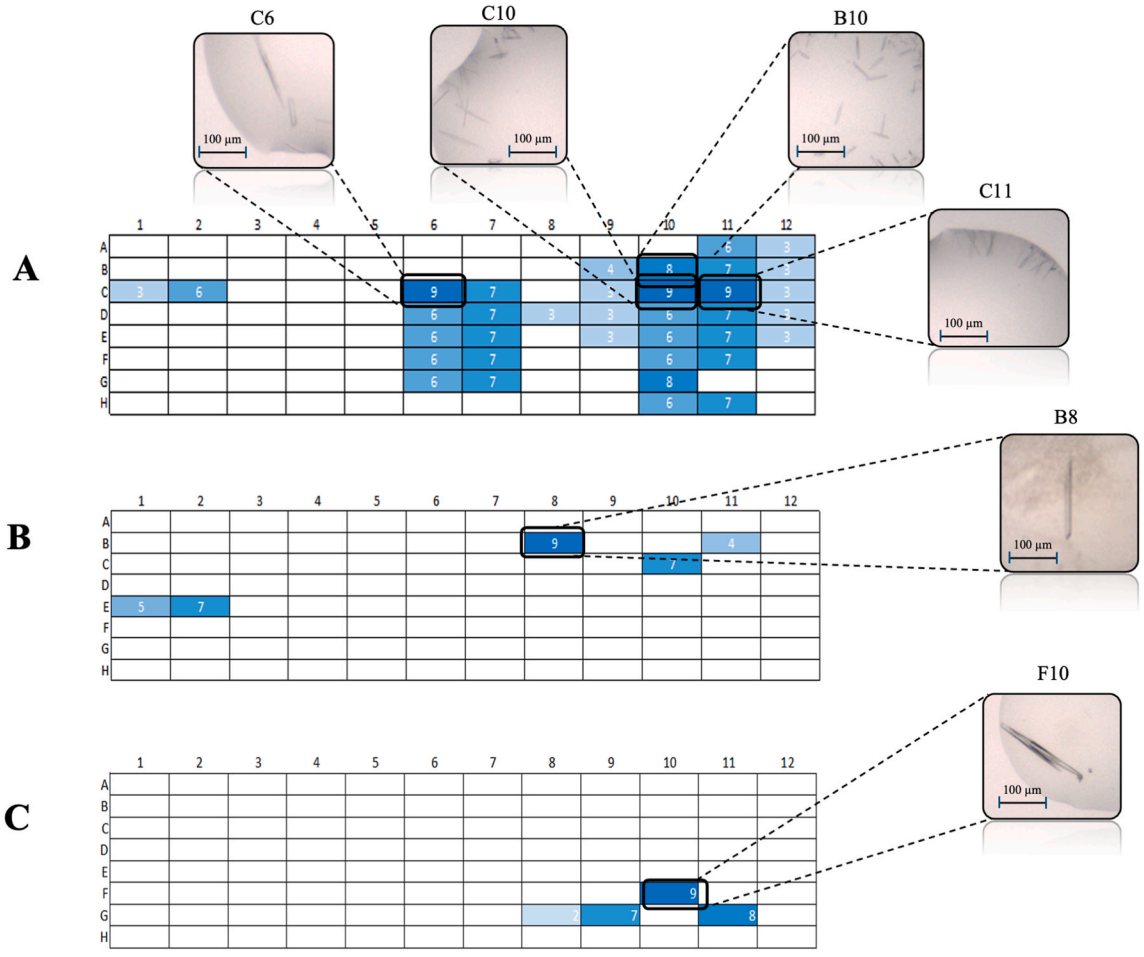


**Fig. 1.** Schematic overview of ALDH1A2 crystallisation screening using a nanolitre drop setup. Coloured cells represent conditions that produced protein crystals; increasing colour intensity corresponds to fewer but larger crystals. Insets show representative crystal formations from the most successful conditions in the following screens: A) Morpheus, B) Wizard 3 + 4, and C) PGA. (For interpretation of the references to colour in this figure legend, the reader is referred to the Web version of this article.)

4000 also provided effective cryoprotection, reducing the risk of damage during handling.

Despite the isoelectric point of ALDH1A2 (pI = 6.17), crystals consistently formed at pH values between 7.5 and 8.5, which we propose as the optimal pH window for crystallisation. Additionally, the inclusion of dithiothreitol (DTT) in the buffer was found to stabilise the catalytic site and reduce protein aggregation.

Our most promising apo-ALDH1A2 crystals (Fig. 1A) appeared within 48 h in two separate experiments using the same precipitant formulation but different protein-to-precipitant ratios (1:1 and 1:0.5 respectively). These findings underscore the importance of fine-tuning precipitant composition and properties to achieve successful crystallisation. Moreover, given the complexity of the Morpheus screen, further optimisation may be achieved by selectively modulating individual components.

Crystals reached their maximum size (approximately 100 μm in the longest direction) within one week and were harvested directly for cryocooling in liquid nitrogen for X-ray diffraction experiments. The highest resolution obtained from the apo-ALDH1A2 crystals was 2.8 Å. While this resolution is modest for large-scale drug discovery applications, it nonetheless represents a significant advancement, as it is the first reported structure of ALDH1A2 in the complete absence of both substrate and cofactor.

This structure complements the previously available $NAD^+$-bound ALDH1A2 structure (PDB: 4X2Q, 2.94 Å resolution), offering new insights into the unliganded conformation of the enzyme. Since ligand-bound structures typically exhibit higher resolution than their apo counterparts, we hypothesise that subtle active-site interactions may contribute to stabilising the overall protein fold or modulating dynamics critical for crystal packing.

The ability to generate crystals from nanolitre-scale droplets is particularly valuable, as it enables rapid and efficient optimisation of crystallisation conditions. This approach can facilitate improvements in crystal morphology and size, leading to better-diffracting crystals while requiring minimal proteins quantities and offering enhanced reproducibility.

This approach allowed us to evaluate the effects of microseeding [34], in which pre-formed microcrystals were introduced into fresh drops. This method is a well-established procedure for controlling nucleation and usually promotes the growth of more ordered crystals, potentially yielding better diffracting samples, suitable for soaking or co-crystallisation with small molecules.

Since many ligands are dissolved in solvents such as DMSO or DMF, we also tested the direct addition of low concentrations of these solvents to assess the tolerance of the crystals. This step is critical for determining the suitability of the system for high-throughput drug-discovery campaigns [35].

### 3.2. *ALDH1A3 crystallisation*

During the crystallisation of ALDH1A3, we observed significant variability in crystal formation across different drops. Notably, both the choice of plate sealing method and the presence of cofactors had a pronounced impact on crystal morphology (Fig. 2), and the overall propensity for crystal growth.

The crystal form shown in Fig. 2B was particularly sensitive to subtle changes in the sealing method adopted. These crystals were initially observed when coverslips were kept in place using adhesive tape rather than tightly sealed. Attempts to reproduce this morphology using conventional sealing greases were unsuccessful. This suggests that complete isolation of the crystallisation drops (such as that achieved with high-vacuum grease) may inhibit crystal formation, whereas a less restrictive seal allows for reproducible growth of birefringent crystals within one week.

Minor changes in the vapour diffusion process likely affect the evaporation rate, making this a critical parameter when exploring the crystallisation space. We found that a slight transpiration, as achieved by loosely sealed coverslips (*e.g.,* using only adhesive tape) enhances crystal quality, we hypothesise that this effect results from a gradual dehydration coupled with the vapour equilibrium, allowing the drop crystallisation drops to reach a favourable crystallisation endpoint. This condition led to a distinct crystal morphology, improved crystal packing, and enhanced diffraction quality.

This form of controlled dehydration may also benefit the crystallisation of other proteins, particularly when traditional vapour diffusion methods fail to optimise crystal properties. However, because the system is not fully sealed, it is essential to harvest crystals promptly to prevent over-dehydration.

Similar evaporation effects may also be induced using semi-permeable sealing techniques, such as mixtures of perspirant greases, and could be adapted for use in microbatch or vapour-batch crystallisation formats.

The different crystal morphologies displayed in Fig. 2 were obtained using the same precipitant, both in the absence and in the presence of the cofactor $NAD^+$. The needle-shaped crystals formed in the absence of cofactors could be optimised to yield 200 μm-long rods (Fig. 2A) in 1 μL + 1 μL hanging drops. Unfortunately, despite their promising morphology, all the crystals diffracted very weakly, possibly due to the loose crystal packing, as none of the cryoprotectants tested improved the diffraction properties.

The second morphology (Fig. 2B and C) was observed when $NAD^+$ was pre-incubated with ALDH1A3 and co-crystallised with the protein. In this case, we obtained either single rounded crystals resembling rice grains (Fig. 2B) or clusters thereof (Fig. 2C). In all instances, their maximum dimension was approximately 100 μm and presented a flat, two-dimensional morphology upon harvesting. These crystals produced high-quality X-ray diffraction data, with resolutions consistently in the range of 2.0–2.5 Å. As the reservoir solution in this condition contained

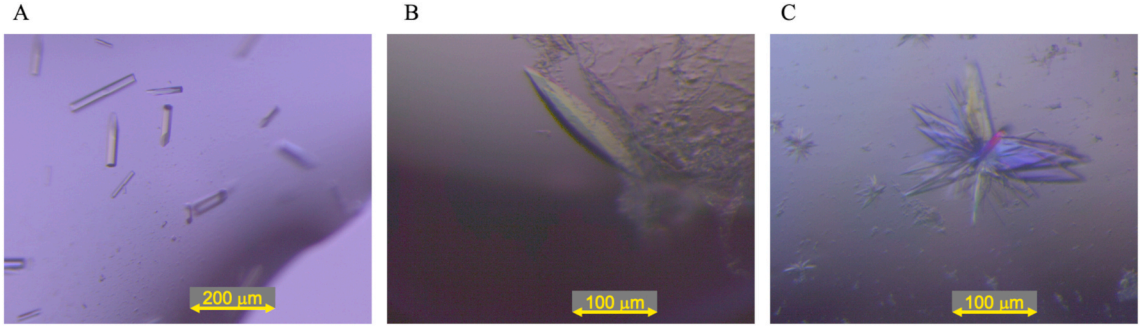


**Fig. 2.** Three images illustrating the various morphologies of ALDH1A3 crystals formed using the same precipitant: A) needle-shaped apo-ALDH1A3 crystals, B) rice grain-shaped $NAD^+$-bound ALDH1A3 crystals, and C) clustered rice grain-shaped $NAD^+$-bound ALDH1A3 crystals.

a significant amount of low-molecular-weight organic precipitant (PEG400), no additional cryoprotection steps were needed prior to harvesting.

The results highlight the importance of selecting the appropriate crystal morphology to consistently achieve high-resolution diffraction data.

Independently of the sealing methods, we unequivocally found that, for ALDH1A3 as well, the presence of a cofactor favours the formation of highly ordered crystals. This observation is supported by the literature in which all crystal structures except for one (PDB 7QK7) contain a cofactor in the binding site, helping to stabilise the protein structure.

As observed in other $NAD^+$-binding proteins, including members of the ALDH family, our electron density maps confirm the clear binding mode for the adenosine part of the cofactor. As the nicotinamide portion appears more flexible and less ordered, likely due to its rotational freedom, we proposed a model reflecting the two possible interpretations: while in monomer A we included all atoms of the cofactor, in monomer B we removed 9 atoms corresponding to the nicotinamide which was not identifiable within the electron density maps. In the first case, the elevated B-factors within the nicotinamide region, compensate for the uncertain position of the atoms, a feature commonly reported in previous ALDH structures [8,36].

Although our dataset has a lower resolution than the equivalent structure reported by Castellví and coworkers [21], the positioning of the adenine moiety is well supported by the electron density maps. These are shown for the $NAD^+$-binding region for both chains of the asymmetric unit (Supplementary Fig. S5A and S5B). The quality of these maps is comparable to those derived from the reprocessed PDB entry 7QK8 using PDB-REDO (Supplementary Fig. S5C and S5D). We attribute this similarity to the high data redundancy in our ALDH1A3 structure (multiplicity >13) and propose to overcome limitations in resolution by increasing the reciprocal space sampling, eventually also by considering multi-axis goniometry for data collection.

Importantly, our structure does not show significant deviations from ATP-bound ALDH1A3 structure available in the Protein Data Bank. This consistency reinforces the notion that the adenosine-binding pocket is well-defined and structurally conserved, while the flexibility of the nicotinamide moiety likely reflects its dynamic role in catalysis.

Nonetheless, electron densities of good quality can be achieved, and the active site is well defined also in the experimental conditions described here. The crystallisation and data collection methods described here have yielded consistently interpretable maps in the presence of ligands from various families and can be extended to small structure based drug discovery campaigns.

### 3.3. *Effects of co-factor binding to ALDH1A2 and ALDH1A3*

Our investigation into the structure-function relationships of $NAD^+$ binding to ALDH1A2 and ALDH1A3 began with an SPR kinetic analysis (Fig. 3), which revealed distinct differences in cofactor affinity between the two isoforms. While both enzymes are capable of binding $NAD^+$, ALDH1A3 exhibits significantly higher affinity ($K_d$ = 33 nM) compared to ALDH1A2, ($K_d$ = 16.8 μM). These findings suggest that $NAD^+$ not only plays a central role in the ALDH1A3's enzymatic activity but also contributes substantially to its structural stabilisation.

To further explore the role of $NAD^+$ and gain insight into the ALDH1A2 active site, we present the first structure of the enzyme in its unliganded (apo) form. Unlike most ligand-bound ALDH structures in the Protein Data Bank, the apo-ALDH1A2 crystallised in the monoclinic space-group $P2_1$, with four monomers in the asymmetric unit (Fig. 4).

A notable feature of our ALDH1A2 crystals is the weak electron density observed in the loop spanning residues 475–497, consistent with the previously unpublished $NAD^+$-bound structure (PDB: 4X2Q). Although this loop has been reported to interact with residues 162–166 of a neighbouring monomer, our SEC elution profiles show that apo-ALDH1A2 adopts a tetrameric arrangement (Fig. S6), suggesting that these loop-mediated contacts are not essential for oligomerisation. The pronounced flexibility of loop 475–497 appears to be a unique feature of

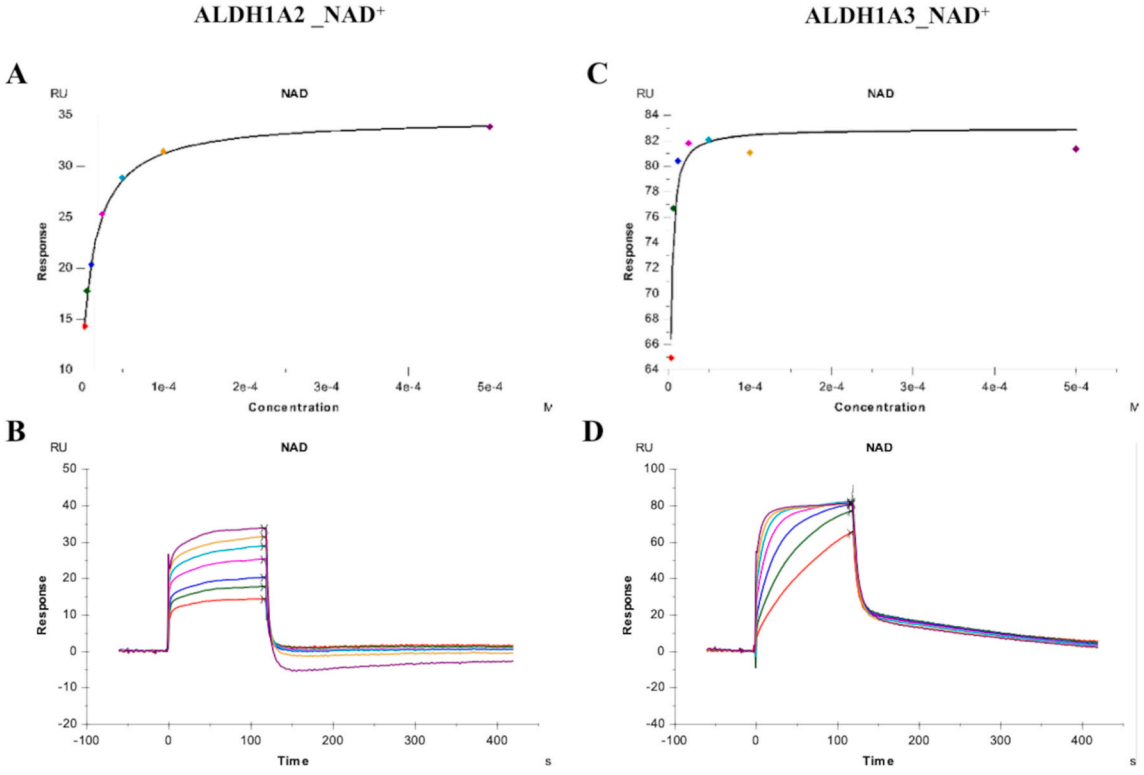


**Fig. 3.** SPR analysis of the dissociation constant ($K_d$) for the interaction between $NAD^+$ and ALDH1A subtypes. A) Equilibrium binding response of ALDH1A2 to $NAD^+$, and B) its corresponding sensorgram (time-dependent response curve). C) and D) show the equivalent data for ALDH1A3.

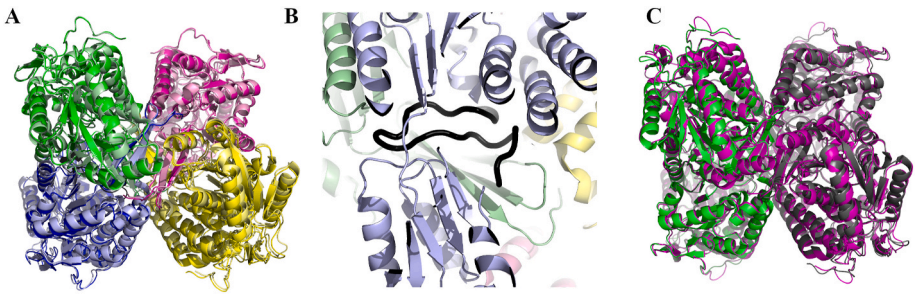


**Fig. 4.** Oligo-tetrameric structure of human ALDH1A2. A) Ribbon representation of the ALDH1A2 tetramer with individual subunits coloured (yellow: chain A, green: chain B, magenta: chain C, blue: chain D). N-terminal tails extend outward, while C-termini are buried within the tetramer core. B) The interactions between the loop region (residues 475–497, in black) and the surrounding structure as presented in the structures in which the loop is stabilised. C) Structural overlay of dimeric ALDH1A3 (PDB: 7QK9, green) and its symmetry mate (grey) with tetrameric ALDH1A2 (PDB: 6ALJ, magenta). (For interpretation of the references to colour in this figure legend, the reader is referred to the Web version of this article.)

ALDH1A2 and may present an opportunity for designing isoform-specific ligands that extend into this otherwise inaccessible region, which is more rigid in other ALDH isoforms. Notably, the highest-resolution structures of ALDH1A2 reported to date by Chen and colleagues have all been determined in the presence of ligands that interact with the flexible loop, stabilising it in a well-defined conformation [18].

Instead, the broader C-terminal region (residues 468–512) forms extensive interactions with the corresponding region of an adjacent monomer. Additional inter-subunit contacts are formed between α-helices spanning residues 266–278 (Fig. 4B).

The overall fold of ALDH1A2 remains largely unchanged in the absence of its co-factor. However, monoclinic crystals (space-group $P2_1$) consistently produced better diffraction quality than their orthorhombic counterparts (space-group $P2_12_12_1$). Achieving reproducible crystallisation of ALDH1A2 in this optimal form using nanolitre-scale drops represents a significant advancement, enabling large-scale ligand-binding studies targeting this enzyme.

Importantly, the conformation of the flexible loop region (residues 475–497) does not interfere with tetramer formation. This opens the possibility of co-crystallisation or soaking experiments with ligands or fragments that target either of the loop's conformational states.

Since apo crystals often exhibit poor diffraction, we recommend pre-incubating the protein with cofactors such as $NAD^+$ or weaker, displaceable analogues prior to crystallisation. This strategy can stabilise the active site and promote improved crystal packing, particularly beneficial for soaking experiments aimed at the co-factor binding site.

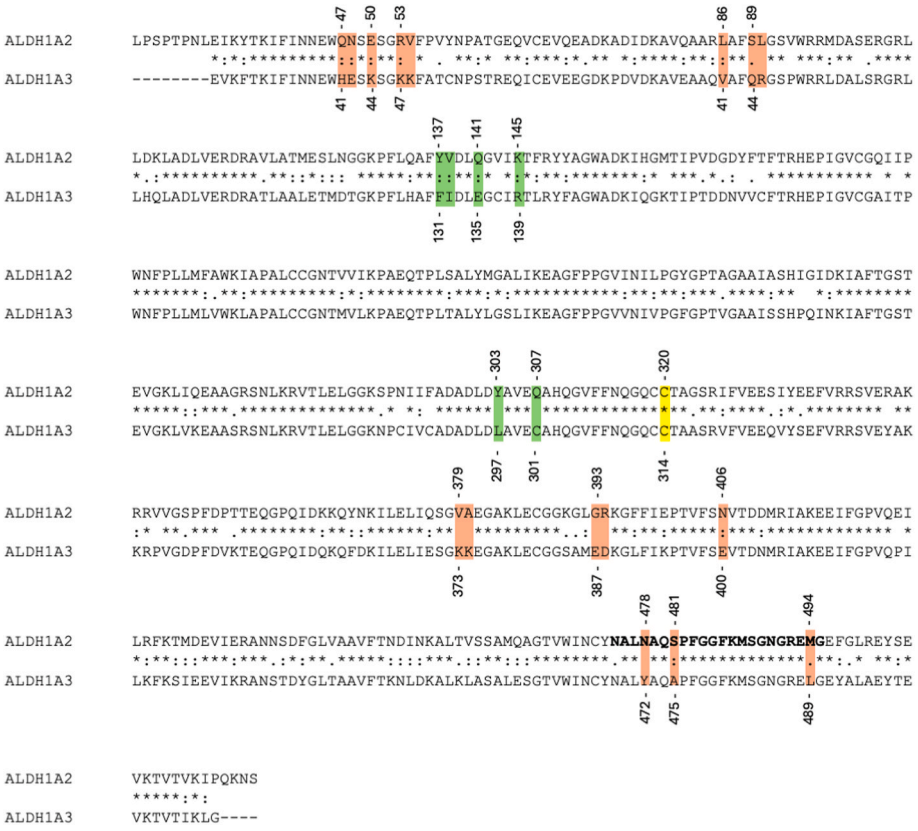


**Fig. 5.** Sequence alignment of human ALDH1A2 and ALDH1A3. Key surface residues involved in crystal packing are highlighted in orange, while catalytic site residues are shown in green. The catalytic cysteine is indicated in yellow, and the flexible loop (absent in the apo-ALDH1A2 structure) is marked in bold. (For interpretation of the references to colour in this figure legend, the reader is referred to the Web version of this article.)

### 3.4. Extending ALDH1A2 crystallisability to ALDH1A3

As previously discussed, the crystallisation of ALDH1A3 is highly sensitive to experimental setup conditions, and to date, we have not yet succeeded in generating crystals from nanolitre-scale drops. In contrast, ALDH1A2 consistently yields crystals under these conditions. This observation suggests two complementary strategies to extend high throughput crystallisability to ALDH1A3.

The first strategy involves engineering ALDH1A2 to mimic the substrate-binding characteristics of ALDH1A3. This approach could enable the use of ALDH1A2 as a structural scaffold for ligand-binding studies targeting ALDH1A3. Given the high degree of structural similarity between the two isoforms particularly in the active site (Fig. 5) this mutagenesis-based method could facilitate parallel structure-based drug discovery campaigns. However, the flexible loop spanning residues 475–497 in ALDH1A2, which differs significantly from the more rigid, 'locked' conformation observed in ALDH1A3, must be considered. To address this, a full loop transplant from ALDH1A3 into ALDH1A2 may be necessary, although such a modification could unpredictably affect the protein's flexibility and crystallisation behaviour.

Specific mutations proposed to remodel the ALDH1A2 active site include V132I, Q135E, K139R, and F137Y within one α-helix, and Y297L and Q301C within another In the flexible loop region, N472Y, S475A and M488L are likely to influence ligand binding and loop stability [37]. These mutations are showed in Fig. 6A.

The second strategy focuses on modifying surface-exposed residues of ALDH1A3 to mimic those of ALDH1A2, with the goal of improving crystal packing and contact formation. This surface residue borrowing" approach is depicted in Fig. 6B. Key mutations in the N-terminal region include H41Q, E42 N, K44E, K47R, and K48V. More Additional differences in the 373–400 region K373V, K374A, E387G, D388R, E400 N may also contribute to improved crystallisability. Although V80L, Q83S, and R84L are oriented internally within the ALDH1A3 tetramer, they may still influence overall packing and should be considered.

Among the proposed mutations, those that alter surface charge or target flexible residues, particularly lysines, are known to enhance crystal packing. Furthermore, surface lysine methylation has been successfully proven to improve crystallisation in other systems [38]. While this technique is more challenging to standardise, it be valuable for generating for generating high quality crystal seeds.

## 4. Conclusions

This study describes the first crystallographic structure of apo-ALDH1A2, shedding new light on the future of drug discovery targeting this class of enzymes.

We provide evidence that the crystallisation of this enzyme can be streamlined using nanolitre-sized drops deposited by robotic equipment. This approach is essential for enabling high-throughput crystallographic screening of large compound libraries, including fragment-based drug discovery strategies [35] or *in situ* data collection [39].

Based on our findings with ALDH1A2, we propose mutagenesis-based strategies to generate mimics of the ALDH1A3 active site with an enhanced propensity for crystallisation. This could pave the way to the design of isoform-selective compounds aimed at treating a wide range of pathologies.

## PDB accession codes

The structures in this work have been deposited in the Protein Data Bank with accession 9R3Z (for ALDH1A2) and 9QZE (for ALDH1A3).

## CRediT authorship contribution statement

**Sonia Siragusa:** Writing – review & editing, Writing – original draft, Visualization, Investigation. **Silvia Garavaglia:** Writing – review & editing, Writing – original draft, Validation, Supervision, Resources, Investigation, Funding acquisition, Conceptualization. **Marco Mazzorana:** Writing – review & editing, Writing – original draft, Validation, Supervision, Resources, Methodology, Investigation, Conceptualization.

## Declaration of generative AI in scientific writing

The authors made use of AI tools (Microsoft Copilot and Grammarly) to improve grammar, spelling, and readability. No generative AI was used in the conceptualization, design, analysis, or creation of the scientific content of this work. Similarly, no generative AI tools were used for image generation, modification, or reprocessing.

## Funding

This work was supported by the European Union –Next Generation EU [PNRRM6C2–12376588 to S.G]. The authors would like to thank Diamond Light Source for the beamtime (proposal MX39345), and the staff of beamline I04 for their assistance with crystal testing and data collection. Dr Sonia Siragusa holds a career grant supported by the European Commission – FSE REACT-EU, PON Research and Innovation 2014–2020.

## Declaration of competing interest

The authors declare the following financial interests/personal

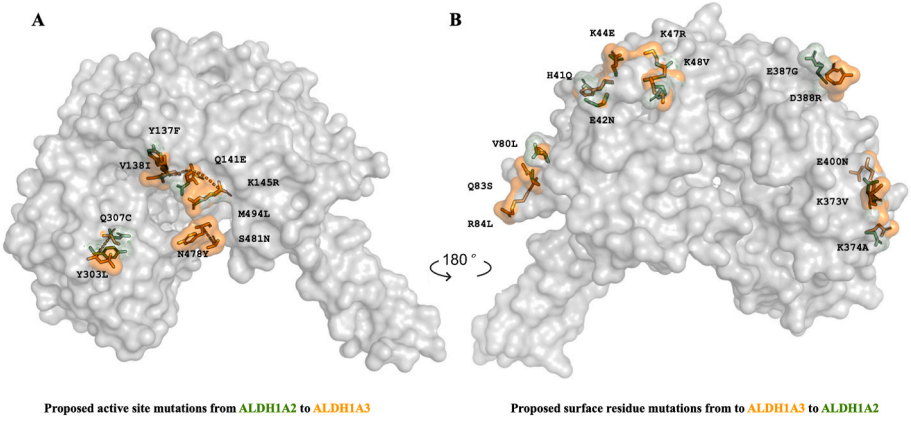


**Fig. 6.** Spatial distribution of proposed mutations mapped onto the 3D structure of the protein. A) Residues in the active site of ALDH1A2 (green) to mutate to mimic the ligand-binding characteristics of those in ALDH1A3 (orange). B) Surface residues of ALDH1A3 to mutate to those of ALDH1A2 to improve crystallisability. (For interpretation of the references to colour in this figure legend, the reader is referred to the Web version of this article.)

relationships which may be considered as potential competing interests: Silvia Garavaglia reports financial support was provided by Italy Ministry of Health Directorate General of Health Prevention. Silvia Garavaglia reports equipment, drugs, or supplies was provided by Diamond Light Source Ltd. Sonia Siragusa reports financial support was provided by European Commission. Silvia Garavaglia has patent #WO2022214995A1 issued to Universita' Degli Studi Del Piemonte Orientale "A. Avogadro", Universita' Degli Studi Di Pavia. If there are other authors, they declare that they have no known competing financial interests or personal relationships that could have appeared to influence the work reported in this paper.

## Acknowledgements

We wish to thank Dr. Gemma Harris (Research Complex at Harwell) for the assistance in the collection and analysis of SPR data.

We thank Prof. Davide Ferraris for the generation of the graphical abstract using BioRender (licensed to Ferraris, D. (2025) https://BioRender.com/w93k672).Figs. 4 and 6 were generated using PyMOL [40].

## Appendix A. Supplementary data

Supplementary data to this article can be found online at https://doi.org/10.1016/j.bbrc.2025.152469.

## References

[1] P. Sinharoy, S.L. McAllister, M. Vasu, E.R. Gross, Environmental aldehyde sources and the health implications of exposure, Adv. Exp. Med. Biol. 1193 (2019) 35–52, https://doi.org/10.1007/978-981-13-6260-6_2.

[2] V. Vasiliou, A. Pappa, T. Estey, Role of human aldehyde dehydrogenases in endobiotic and xenobiotic metabolism, Drug Metab. Rev. 36 (2004) 279–299, https://doi.org/10.1081/dmr-120034001.

[3] V. Vasiliou, A. Bairoch, K.F. Tipton, D.W. Nebert, Eukaryotic aldehyde dehydrogenase (ALDH) genes: human polymorphisms, and recommended nomenclature based on divergent evolution and chromosomal mapping, Pharmacogenetics 9 (1999) 421–434.

[4] V. Vasiliou, D.W. Nebert, Analysis and update of the human aldehyde dehydrogenase (ALDH) gene family, Hum. Genomics 2 (2005) 138, https://doi.org/10.1186/1479-7364-2-2-138.

[5] C.-H. Chen, B.R. Kraemer, L. Lee, D. Mochly-Rosen, Annotation of 1350 common genetic variants of the 19 ALDH multigene family from global human genome aggregation database (gnomAD), Biomolecules 11 (2021) 1423, https://doi.org/10.3390/biom11101423.

[6] Z.-J. Liu, Y.-J. Sun, J. Rose, Y.-J. Chung, C.-D. Hsiao, W.-R. Chang, I. Kuo, J. Perozich, R. Lindahl, J. Hempel, B.-C. Wang, The first structure of an aldehyde dehydrogenase reveals novel interactions between NAD and the rossmann fold, Nat. Struct. Biol. 4 (1997) 317–326, https://doi.org/10.1038/nsb0497-317.

[7] C.G. Steinmetz, P. Xie, H. Weiner, T.D. Hurley, Structure of mitochondrial aldehyde dehydrogenase: the genetic component of ethanol aversion, Structure 5 (1997) 701–711, https://doi.org/10.1016/s0969-2126(97)00224-4.

[8] A. Moretti, J. Li, S. Donini, R.W. Sobol, M. Rizzi, S. Garavaglia, Crystal structure of human aldehyde dehydrogenase 1A3 complexed with NAD+ and retinoic acid, Sci. Rep. 6 (2016) 35710, https://doi.org/10.1038/srep35710.

[9] S.A. Marchitti, C. Brocker, D. Stagos, V. Vasiliou, Non-P450 aldehyde oxidizing enzymes: the aldehyde dehydrogenase superfamily, Expert Opin. Drug Metab. Toxicol. 4 (2008) 697–720, https://doi.org/10.1517/17425255.4.6.697.

[10] V. Koppaka, D.C. Thompson, Y. Chen, M. Ellermann, K.C. Nicolaou, R.O. Juvonen, D. Petersen, R.A. Deitrich, T.D. Hurley, V. Vasiliou, Aldehyde dehydrogenase inhibitors: a comprehensive review of the pharmacology, mechanism of action, substrate specificity, and clinical application, Pharmacol. Rev. 64 (2012) 520–539, https://doi.org/10.1124/pr.111.005538.

[11] J.E. Balmer, R. Blomhoff, Gene expression regulation by retinoic acid, J. Lipid Res. 43 (2002) 1773–1808, https://doi.org/10.1194/jlr.R100015-JLR200.

[12] G. Duester, Retinoic acid synthesis and signaling during early organogenesis, Cell 134 (2008) 921–931, https://doi.org/10.1016/j.cell.2008.09.002.

[13] K.M.C. Mohammad Sultan, Retinoid signaling in cancer and its promise for therapy, J. Carcinog. Mutagen. (2013), https://doi.org/10.4172/2157-2518.S7-006.

[14] J. Li, S. Garavaglia, Z. Ye, A. Moretti, O.V. Belyaeva, A. Beiser, M. Ibrahim, A. Wilk, S. McClellan, A.V. Klyuyeva, K.R. Goggans, N.Y. Kedishvili, E.A. Salter, A. Wierzbicki, M.E. Migaud, S.J. Mullett, N.A. Yates, C.J. Camacho, M. Rizzi, R. W. Sobol, A specific inhibitor of ALDH1A3 regulates retinoic acid biosynthesis in glioma stem cells, commun, Biol 4 (2021) 1–16, https://doi.org/10.1038/s42003-021-02949-7.

[15] H. Tomita, K. Tanaka, T. Tanaka, A. Hara, Aldehyde dehydrogenase 1A1 in stem cells and cancer, Oncotarget 7 (2016) 11018–11032, https://doi.org/10.18632/oncotarget.6920.

[16] L. Magrassi, G. Pinton, S. Luzzi, S. Comincini, A. Scravaglieri, V. Gigliotti, B. L. Bernardoni, I. D'Agostino, F. Juretich, C. La Motta, S. Garavaglia, A new vista of aldehyde dehydrogenase 1A3 (ALDH1A3): new specific inhibitors and activity-based probes targeting ALDH1A3 dependent pathways in glioblastoma, mesothelioma and other cancers, Cancers 16 (2024) 2397, https://doi.org/10.3390/cancers16132397.

[17] G. Budziszewski, M. Snell, T. Wright, M. Lynch, S. Bowman, High-throughput screening to obtain crystal hits for protein crystallography, J. Vis. Exp. (2023), https://doi.org/10.3791/65211.

[18] Y. Chen, J.-Y. Zhu, K.H. Hong, D.C. Mikles, G.I. Georg, A.S. Goldstein, J.K. Amory, E. Schönbrunn, Structural basis of ALDH1A2 inhibition by irreversible and reversible small molecule inhibitors, ACS Chem. Biol. 13 (2018) 582, https://doi.org/10.1021/acschembio.7b00685.

[19] L. Quattrini, E.L.M. Gelardi, V. Coviello, S. Sartini, D.M. Ferraris, M. Mori, I. Nakano, S. Garavaglia, C. La Motta, Imidazo[1,2-a]pyridine derivatives as aldehyde dehydrogenase inhibitors: novel chemotypes to target glioblastoma stem cells, J. Med. Chem. 63 (2020) 4603–4616, https://doi.org/10.1021/acs.jmedchem.9b01910.

[20] E.L.M. Gelardi, G. Colombo, F. Picarazzi, D.M. Ferraris, A. Mangione, G. Petrarolo, E. Aronica, M. Rizzi, M. Mori, C. La Motta, S. Garavaglia, A selective competitive inhibitor of aldehyde dehydrogenase 1A3 hinders cancer cell growth, invasiveness and stemness in vitro, Cancers 13 (2021) 356, https://doi.org/10.3390/cancers13020356.

[21] A. Castellví, R. Pequerul, V. Barracco, J. Juanhuix, X. Parés, J. Farrés, Structural and biochemical evidence that ATP inhibits the cancer biomarker human aldehyde dehydrogenase 1A3, Commun. Biol. 5 (2022) 1–12, https://doi.org/10.1038/s42003-022-03311-1.

[22] F. Gorrec, The MORPHEUS protein crystallization screen, J. Appl. Crystallogr. 42 (2009) 1035–1042, https://doi.org/10.1107/S0021889809042022.

[23] T.-C. Hu, J. Korczyńska, D.K. Smith, A.M. Brzozowski, High-molecular-weight polymers for protein crystallization: poly-γ-glutamic acid-based precipitants, Acta Crystallogr. D Biol. Crystallogr. 64 (2008) 957–963, https://doi.org/10.1107/S0907444908021616.

[24] G. Winter, D.G. Waterman, J.M. Parkhurst, A.S. Brewster, R.J. Gildea, M. Gerstel, L. Fuentes-Montero, M. Vollmar, T. Michels-Clark, I.D. Young, N.K. Sauter, G. Evans, *Dials* : implementation and evaluation of a new integration package, Acta Crystallogr. Sect. Struct. Biol. 74 (2018) 85–97, https://doi.org/10.1107/S2059798317017235.

[25] G. Winter, J. Beilsten-Edmands, N. Devenish, M. Gerstel, R.J. Gildea, D. McDonagh, E. Pascal, D.G. Waterman, B.H. Williams, G. Evans, DIALS as a toolkit, Protein Sci. Publ. Protein Soc. 31 (2022) 232–250, https://doi.org/10.1002/pro.4224.

[26] E. Krissinel, V. Uski, A. Lebedev, M. Winn, C. Ballard, Distributed computing for macromolecular crystallography, Acta Crystallogr. Sect. Struct. Biol. 74 (2018) 143–151, https://doi.org/10.1107/S2059798317014565.

[27] A.J. McCoy, R.W. Grosse-Kunstleve, P.D. Adams, M.D. Winn, L.C. Storoni, R. J. Read, Phaser crystallographic software, J. Appl. Crystallogr. 40 (2007) 658–674, https://doi.org/10.1107/S0021889807021206.

[28] P.V. Afonine, R.W. Grosse-Kunstleve, N. Echols, J.J. Headd, N.W. Moriarty, M. Mustyakimov, T.C. Terwilliger, A. Urzhumtsev, P.H. Zwart, P.D. Adams, Towards automated crystallographic structure refinement with *phenix.refine*, Acta Crystallogr. D Biol. Crystallogr. 68 (2012) 352–367, https://doi.org/10.1107/s0907444912001308.

[29] P.D. Adams, P.V. Afonine, K. Baskaran, H.M. Berman, J. Berrisford, G. Bricogne, D. G. Brown, S.K. Burley, M. Chen, Z. Feng, C. Flensburg, A. Gutmanas, J.C. Hoch, Y. Ikegawa, Y. Kengaku, E. Krissinel, G. Kurisu, Y. Liang, D. Liebschner, L. Mak, J. L. Markley, N.W. Moriarty, G.N. Murshudov, M. Noble, E. Peisach, I. Persikova, B. K. Poon, O.V. Sobolev, E.L. Ulrich, S. Velankar, C. Vonrhein, J. Westbrook, M. Wojdyr, M. Yokochi, J.Y. Young, Announcing mandatory submission of PDBx/mmCIF format files for crystallographic depositions to the Protein Data Bank (PDB), Acta Crystallogr. Sect. Struct. Biol. 75 (2019) 451–454, https://doi.org/10.1107/s2059798319004522.

[30] P. Emsley, B. Lohkamp, W.G. Scott, K. Cowtan, Features and development of Coot, Acta Crystallogr. D Biol. Crystallogr. 66 (2010) 486, https://doi.org/10.1107/S0907444910007493.

[31] G.N. Murshudov, A.A. Vagin, E.J. Dodson, Refinement of macromolecular structures by the maximum-likelihood method, Acta Crystallogr. D Biol. Crystallogr. 53 (1997) 240–255, https://doi.org/10.1107/S0907444996012255.

[32] A.A. Vagin, R.A. Steiner, A.A. Lebedev, L. Potterton, S. McNicholas, F. Long, G. N. Murshudov, REFMAC5 dictionary: organization of prior chemical knowledge and guidelines for its use, Acta Crystallogr. D Biol. Crystallogr. 60 (2004) 2184–2195, https://doi.org/10.1107/S0907444904023510.

[33] G.G. Langer, S.X. Cohen, V.S. Lamzin, A. Perrakis, Automated macromolecular model building for X-ray crystallography using ARP/wARP version 7, Nat. Protoc. 3 (2008) 1171, https://doi.org/10.1038/nprot.2008.91.

[34] T. Bergfors, Seeds to crystals, J. Struct. Biol. 142 (2003) 66–76, https://doi.org/10.1016/S1047-8477(03)00039-X.

[35] A. Douangamath, A. Powell, D. Fearon, P.M. Collins, R. Talon, T. Krojer, R. Skyner, J. Brandao-Neto, L. Dunnett, A. Dias, A. Aimon, N.M. Pearce, C. Wild, T. Gorrie-Stone, F. von Delft, Achieving efficient fragment screening at XChem facility at diamond light source, J. Vis. Exp. JoVE (2021), https://doi.org/10.3791/62414.

[36] P.K. Hammen, A. Allali-Hassani, K. Hallenga, T.D. Hurley, H. Weiner, Multiple conformations of NAD and NADH when bound to human cytosolic and mitochondrial aldehyde dehydrogenase, Biochemistry 41 (2002) 7156–7168, https://doi.org/10.1021/bi012197t.

[37] L.A. Lipscomb, N.C. Gassner, S.D. Snow, A.M. Eldridge, W.A. Baase, D.L. Drew, B. W. Matthews, Context-dependent protein stabilization by methionine-to-leucine

substitution shown in T4 lysozyme, Protein Sci. Publ. Protein Soc. 7 (1998) 765–773.
[38] T.S. Walter, C. Meier, R. Assenberg, K.-F. Au, J. Ren, A. Verma, J.E. Nettleship, R. J. Owens, D.I. Stuart, J.M. Grimes, Lysine methylation as a routine rescue strategy for protein crystallization, Struct. Lond. Engl. 14 (2006) 1617–1622, https://doi.org/10.1016/j.str.2006.09.005, 1993.
[39] J. Sanchez-Weatherby, J. Sandy, H. Mikolajek, C.M.C. Lobley, M. Mazzorana, J. Kelly, G. Preece, R. Littlewood, T.L.M. Sørensen, VMXi: a fully automated, fully remote, high-flux in situ macromolecular crystallography beamline, J. Synchrotron Radiat. 26 (2019) 291–301, https://doi.org/10.1107/S1600577518015114.
[40] L. Schrödinger, W. DeLano, PyMOL. http://www.pymol.org/pymol,PYMOL, 2020 n.d.